Ge-on-Si Photonics for Mid-infrared Absorption and Sensing Applications

K. Gallacher[1], L. Baldassarre[2,] A. Samarelli[1], R. W. Millar[1], A. Ballabio[3], J. Frigerio[3], G. Isella[3], A. Bashir[4], I. MacLaren[4], G. Pellegrini[5], P. Biagioni[5]. M. Ortolani[2], D. J. Paul[1]

[1]University of Glasgow, School of Engineering, Rankine Building, Oakfield Avenue, Glasgow, G12 8LT, U.K

[2]Center for Life NanoScience@Sapienza, Istituto Italiano di Tecnologia, Viale Regina Elena 291, I-00161 Rome, Italy

[3]L-NESS, Dipartimento di Fisica del Politecnico di Milano, Polo Territoriale di Como, Via Anzani 42, I-22100 Como, Italy

[4]University of Glasgow, School of Physics and Astronomy, Kelvin Building, University Avenue, Glasgow G12 8QQ, U.K..

[5]Dipartimento di Fisica, Politecnico di Milano, Piazza Leonardo da Vinci 32, I-20133 Milano, Italy

ABSTRACT

There is significant interest to develop cheap CMOS compatible sensors that operate in the mid-infrared (MIR). To meet these requirements, Ge-on-Si is proving to be an exciting platform. There is the potential to realize waveguide integrated quantum well infrared photodetectors (QWIPs) based on Ge quantum wells (QWs). Intersubband absorption from p-Ge QWs has been demonstrated in the important atmospheric transmission window of 8-13 μm. An alternative strategy for sensing in the MIR is demonstrated through highly n-type doped Ge plasmonic antennas. These antennas demonstrate vibrational sensing of polydimethylsiloxane (PDMS) spin coated layers at 12.5 μm wavelength. These demonstrate enhanced sensing capabilities due to the localized hot spots of the antenna resonant modes.

INTRODUCTION

There is significant interest to develop cheap and practical detectors that cover the important transmission windows within the mid-infrared (3-5 and 8-13 μm wavelength) to enable on-chip biological and gas sensing spectroscopic detectors. Currently the gold standard for detection at these wavelengths is mercury-cadmium-telluride (MCT) due to the inherently large detectivities from interband absorption [1]. The disadvantages with MCT are that it is fragile, has low process uniformity, is not easily integrated with Si and the toxic elements have been banned for use in civilian products in Europe. InSb gas detectors are now available in the 3 to 5 μm window but the material is fragile and difficult to process [2]. This paper will discuss two potential routes for detection based on the Ge on Si material platform.

Recently it has been demonstrated that p-Ge quantum wells (QWs) can provide strong absorption in the 8-13 μm wavelength range through intersubband absorption [3]. These p-Ge QW superlattice structures can be strain symmetrised past critical thickness limitations and therefore provide large absorption coefficients. Initial experimental results from as-grown p-Ge QW superlattice structures are discussed along with future integration strategies to realise a waveguide coupled quantum well infrared photodetector (QWIP).

An alternative Group IV sensing strategy is to use the plasmonic effect of highly n-type doped Ge in the MIR. It has been demonstrated recently that n-type Ge plasmonic antennas can provide a plasma frequency that resides within the MIR. These can provide localised hot spots that provide over 2 orders of magnitude signal enhancement and sensing has been demonstrated with PDMS at ~ 12.5 μm wavelength [4]. These antennas provide the advantage that the plasmonic response can be tuned by changing the dopant concentration compared to standard metal antennas. Experimental results for the plasmonic resonances for fabricated n-Ge antenna samples are discussed along with future integration strategies.

MID-INFRARED QUANTUM WELLS INTERSUBBAND PHOTODETECTORS

A good candidate for cheap and practical sensors is QWIPs. Since absorption can occur from intersubband transitions within the QW, the absorption can be tuned by adjusting the QW width, thereby changing the energy of the confined subband states. This allows the potential to engineer strong absorption from normally transparent semiconductors such as Si and Ge in the MIR. QWIPs have been previously demonstrated with p and n-type SiGe designs [5, 6]. There has only been one recent demonstration of intersubband absorption from a pure Ge QW (n-type) [7]. The majority of the investigation into Si compatible QWIPs have been limited to low Ge concentration structures. This has been due to the large lattice mismatch of 4.2% between Si and Ge [8]. It is now possible to grow high quality pure Ge QWs on a thin (~1 μm) SiGe strain relaxed virtual substrate [9, 10] using techniques such as low energy plasma enhanced chemical vapour deposition (LEPECVD). The benefit of using p-Ge QWs over p-$Si_{1-x}Ge_x$ QWs for $x < 0.85$ is that it will provide larger absorption coefficients, due to the smaller effective masses for both the heavy hole (HH) and light hole (LH) bands. In addition, whilst conduction band designs only allow TM (z)-polarized intersubband transitions, the valence band allows both TE (x-y) and TM polarizations to be observed [8]. The strain and mixing of the valence band states relax the parabolic selection rules and also provide some TE detection from transitions that only allow TM polarized absorption in the parabolic approximation [8, 11, 12]. Therefore, both surface normal and waveguide geometry devices can be realised that can potentially be built into large arrays. Surface-normal p-type Ge QW intersubband absorption has been experimentally demonstrated for 8.1 nm wide QWs as designed by 8-band **k.p** theory [13]. These are analysed using Fourier transform infrared spectroscopy (FTIR) and scanning transmission electron microscopy (STEM).

QWIP EXPERIMENT

The band energies and confined wave-functions were calculated using a self-consistent 8-band **k.p** Poisson-Schrödinger solver with periodic boundary conditions orientated along the growth-axis and the deformation potentials from ref. [13]. **Figure 1** presents the calculated band structure for an 8.1 nm Ge QW and 5.4 nm $Si_{0.5}Ge_{0.5}$ barriers on a relaxed $Si_{0.2}Ge_{0.8}$ buffer. The ground state in the QW is HH1 due to strain splitting of the HH and LH bands. The HH3 and

LH2 are at roughly the same energy whilst the LH3 states is the first continuum state not confined to the QW. For a doping level of $N_A \approx 10^{18}$ cm^{-3} within the barriers, the Fermi level at room temperature sits between the HH1 and HH2 subbands. Therefore, the HH1-LH2 intersubband transition should be optically active in a surface-normal measurement.

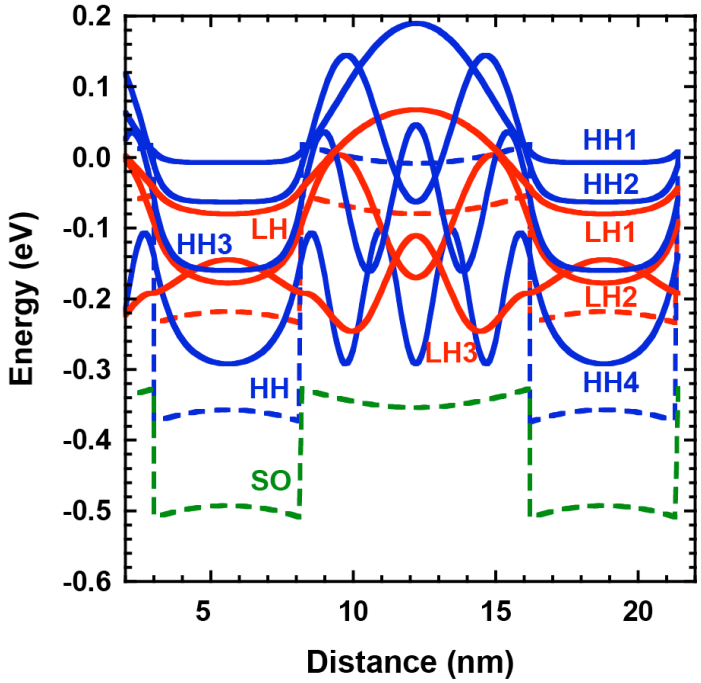

Figure 1. A schematic diagram of the calculated band structure for an 8.1 nm Ge quantum well sandwiched between 5.4 nm $Si_{0.5}Ge_{0.5}$ barriers. The squared wave-functions for the lowest energy subband states for the heavy hole (HH) and light hole (LH) bands are shown.

The designed Ge QW structures were grown by LEPECVD on high resistivity Si (100) to reduce free-carrier absorption from the substrate. A 500 nm thick $Si_{0.6}Ge_{0.4}$ layer was first grown followed by a 500 nm linear graded buffer from x = 0.4 until x = 0.8. Then an undoped 10 nm $Si_{0.2}Ge_{0.8}$ spacer region was grown followed by the active region consisting of 500 periods of compressively strained undoped Ge QWs (and tensile strained p-$Si_{0.5}$ $Ge_{0.5}$ barriers at $N_A \approx 10^{18}$ cm^{-3}) of 8.1 ± 0.5 (5.4 ± 0.6) nm thickness. Lastly, another undoped 10 nm $Si_{0.2}Ge_{0.8}$ spacer layer was grown, followed by a 20 nm $Si_{0.2}Ge_{0.8}$ cap region. Heterolayer thicknesses were measured by STEM. The STEM was performed on a probe-corrected JEOL ARM 200F equipped with a cold field emission gun operated at 200 kV. A Gatan GIF Quantum ER energy filter/ spectrometer equipped with a fast dual electron energy loss spectroscopy (EELS) system was used. The STEM was operated in high angle annular dark field mode (HAADF). Atomic (Z) contrast image was obtained by the detection of elastically and quasi-elastically scattered electrons using a HAADF. Therefore, this is a well suited method for imaging Ge and SiGe interfaces. The HADDF STEM image in **Figure 2** (a) shows the smooth and abrupt interfaces between the Ge QWs and the $Si_{0.5}Ge_{0.5}$ barriers. **Figure 2** (b) reveals that there is a slight variation of the QW and barrier thicknesses throughout the superlattice. The average thickness calculated for the p-Ge QWs is 8.1 ± 0.5 nm and for the $Si_{0.5}$ $Ge_{0.5}$ barriers is 5.4 ± 0.6 nm.

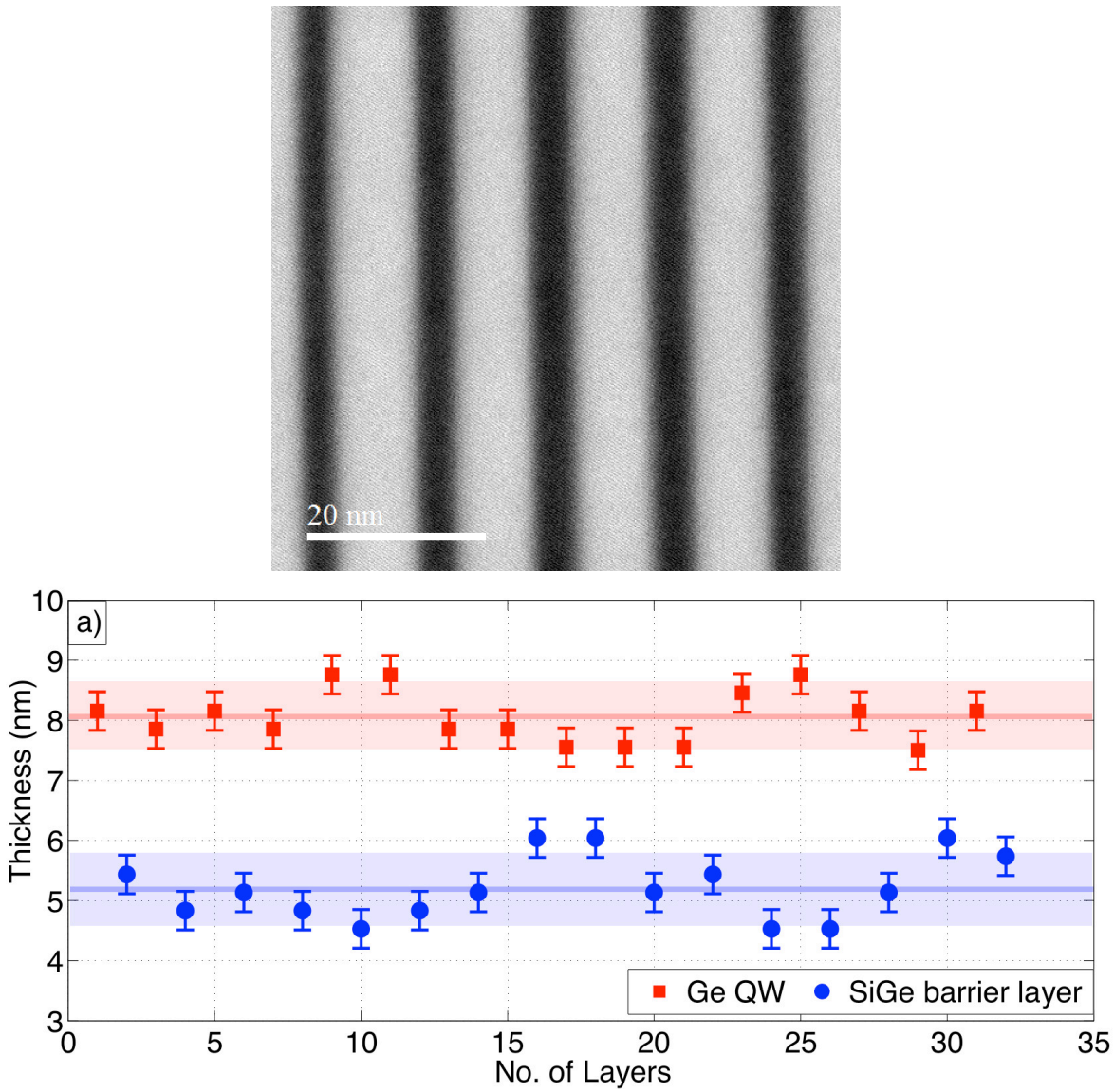

Figure 2. (a) A cross-sectional scanning transmission electron microscope (STEM) image of the 8.1 nm Ge quantum well structure by high angle annular dark field mode STEM image at 3 million times magnification. Due to the Z^2 dependence, heavier atoms appear brighter because of strong scattering at high angles while lighter atoms appear darker. Therefore lighter regions in this image correspond to Ge QWs and the darker regions correspond to the SiGe barriers. (b) Thickness variation of the superlattice structure as obtained from STEM analysis. Ge QWs have an average thickness of 8.1 ± 0.5 nm (red line) and the SiGe barrier are 5.2 ± 0.6 nm thick.

Fourier transform infrared (FTIR) transmission measurements were performed on the as-grown 8.1 nm QW structure in vacuum at temperatures ranging from 6 to 300 K. The setup consisted of a Bruker IFS 66v interferometer and a nitrogen-cooled MCT detector. Blank chips were bonded onto the cold finger of an optical cryostat aligned within the sample chamber of the FTIR. Measurements were performed in surface normal (x-y) geometry with in-plane (TE) light polarization state defined by the properties of the Michelson interferometer. The electric field component parallel to the growth axis (TM) was null at all wavelengths before hitting the sample, but due to the refractive index variation of the complete structure and the backside of the

substrate being unpolished, there will be some scattering that couples some of the radiation into TM polarized active transitions, so both TE and TM transitions will be observed [11] [12]. The normalized FTIR absorption spectra at 300 K in vacuum for the 8.1 nm QW structure is demonstrated in **Figure 3** (a). The narrow absorption peak at ~ 9 µm wavelength corresponds to vibrational interstitial oxygen impurities in the Si substrate [14]. The QW design was for a bound-to-continuum transition from the HH1 to the HH continuum is observed at ~ 3 µm wavelength. As expected, the bound-to-bound transition from the TE polarized HH1 to LH2 transition is the strongest experimentally. The modelled absorption for an ideal TM and TE polarized light beam is also shown. The model agrees reasonably well with the experimental peak positions but at present underestimates the absorption width designs due the modelling not being able to account for broadening effects such as inhomogeneous broadening. The low temperature (6-200 K) absorption spectra of the 8.1 nm QW structure is demonstrated in **Figure 3** (b).

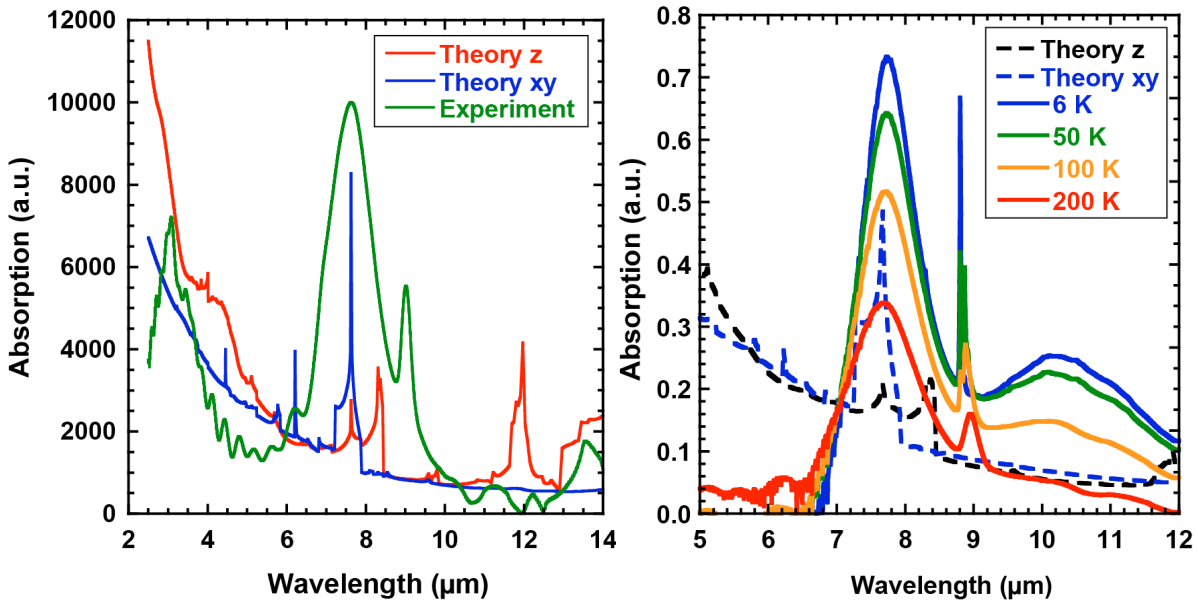

Figure 3. (a) Fourier transform infra-red (FTIR) absorption spectra at 300 K under vacuum for the as-grown 8.1 nm Ge quantum well (QW) structure. The modelled intersubband absorption spectra for TM and TE transitions is also displayed. (b) The low temperature FTIR absorption spectra of the 8.1 nm QW structure from 6-200 K with the theory for both polarizations also included.

In this instance the absorption peak from the Si-O interstitial defect at ~ 9 µm wavelength can be used as a temperature reference since it blue shifts with decreasing temperature and begins to exhibit a narrow line-width below 10 K [14], which is evident in the 6 K spectra. It is clear from **Figure 3** (b) that as the temperature decreases the intersubband absorption is increasing. There is a negligible intersubband absorption temperature dependence observed. This arises from the band-edges of both the barriers and the QWs changing at approximately the same rate in energy as a function of temperature and produce a negligible change in terms of the QW depth for both the HH and LH bands.[15] It is also evident from the spectra that there is a longer wavelength absorption peak appearing with decreasing temperature at ~ 10.2 µm wavelength. Most likely, the Fermi level enters the HH1 subband at low temperature, activating the HH1-HH2 transition. Doping-dependent analysis will be required to address this point further.

HIGHLY N-TYPE DOPED GE PLASMONIC ANTENNAS FOR MIR SENSING

Plasmonic devices allow the increase of the interaction of light with matter. To date, surface plasmon polaritons and localized surface plasmons have been almost exclusively based on metals such as gold, aluminium and silver, which display plasma frequencies close to the visible and near infrared spectral region. At these wavelengths, surface plasmons have shown interesting properties to enable future communication architectures, high performance sensors and high resolution systems [16-21]. Of particular interest could be the extension of these properties to other wavelength regions such as the MIR [22-25]. The reason behind this is that many molecules have vibrational resonances with fingerprints in the atmospheric transmission window of 8-13 μm wavelength [4]. One of the main challenges, to enable MIR plasmonics, is related to the fundamental properties of the commonly used metals, which radically change their properties in the wavelength region of interest. Highly doped semiconductor materials have been suggested as an alternative to metals. Standard doping of semiconductors usually sets the plasma frequency in the far-infrared, whereas high doping levels of ~ 10^{19}-10^{20} cm^{-3} are required for the MIR. Ge has been suggested as suitable plasmonic candidate for the MIR because it is highly transparent. When doped, Ge also has the advantage of a lower effective mass for electrons compared to Si. This is important as the plasma frequency is related to the effective mass of the free carriers. In addition, the possibility to control the carrier density and change the electrodynamic properties makes n-type Ge even more interesting since it will be possible to fine tune the position of the plasma frequency over a wide spectral region [4].

EXPERIMENT

The highly doped n-Ge plasmonic material was epitaxially grown by LEPECVD on a standard Si (001) substrate. Before hetero-epitaxy, the native oxide was removed by dipping the Si in a hydrofluoric acid (HF) solution. The n-Ge was subsequently grown at 500 °C and in-situ doped by phosphine to achieve a doping level of $N_D \sim 2.5 \times 10^{19}$ cm^{-3}. This corresponds to a plasma frequency of ~ 1000 cm^{-1} (~ 10 μm wavelength). Fabrication of the plasmonic n-Ge antennas was achieved by electron beam lithography and an HSQ mask [26]. An inductively coupled plasma tool was used to etch the antennas using a mixed SF_6 and C_4F_8 in a mixed chemistry process [27] which has demonstrated low damage for high quality electrical properties [28]. An SEM image of fabricated 1 μm thick double n-Ge antennas with lengths of 2 μm and a gap of 300 nm is shown in **Figure 4** (a). **Figure 4** (b) shows an angled (85°) close up SEM image of the double antenna. The optimized dry-etch process results in an anisotropic etch profile.

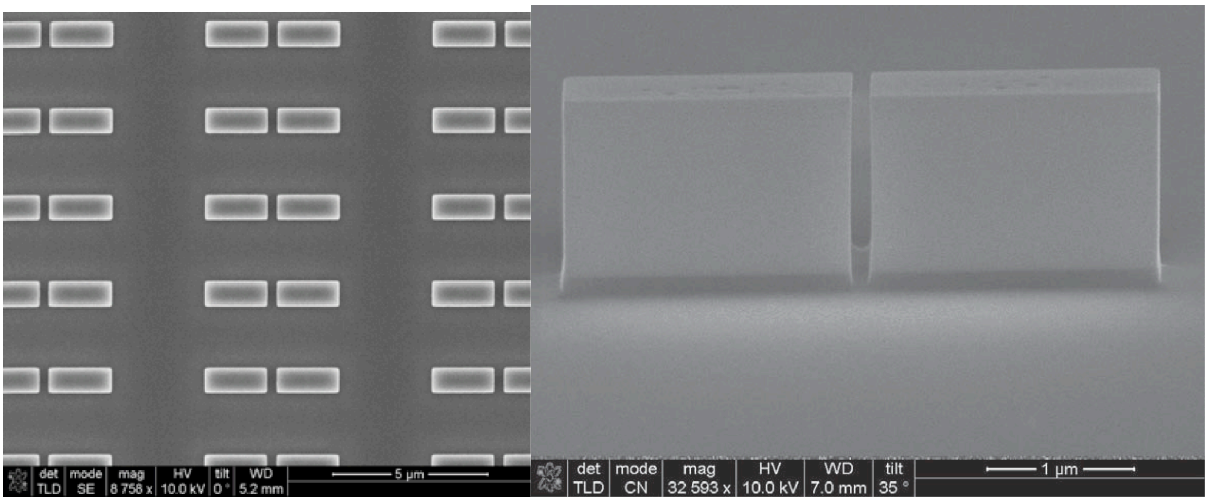

Figure 4. (a) A scanning electron microscope (SEM) image of the fabricated n-Ge plasmonic double antenna array. (b) A close up SEM image of the n-Ge double antennas at ~85° tilt.

The MIR response of the fabricated antennas has been characterized by FTIR. A broadband MIR source was used to illuminate the sample under analysis and the signal was collected with an MCT detector. The absorbance spectra of the antennas are demonstrated in Figure 5. In the following, we identify two different polarizations; co-polarization (co-pol) and cross-polarization (cross-pol), where the field is aligned along or across the antenna arm direction, respectively. The experimental results obtained clearly display a resonance peak R2 at ~ 800 cm^{-1} (12.5 μm wavelength) and R1 at ~ 450 cm^{-1} (~ 22.2 μm wavelength) for the highly doped n-Ge antennas. The undoped reference Ge is also displayed and shows no such resonances. These resonances correspond to hot-spots located at the Ge-air interface [4]. The resonance peaks appear only for the co-pol spectrum of the dipole antenna with high doping (red continuous line). The sharp spectral feature around 610 cm^{-1} (16 μm wavelength) that can be observed in all spectra is due to the Raman-active Si phonon, which couples to IR light because of defects in the Si substrate. The remaining narrow peaks that appear are partly due to impurities in the silicon wafers.

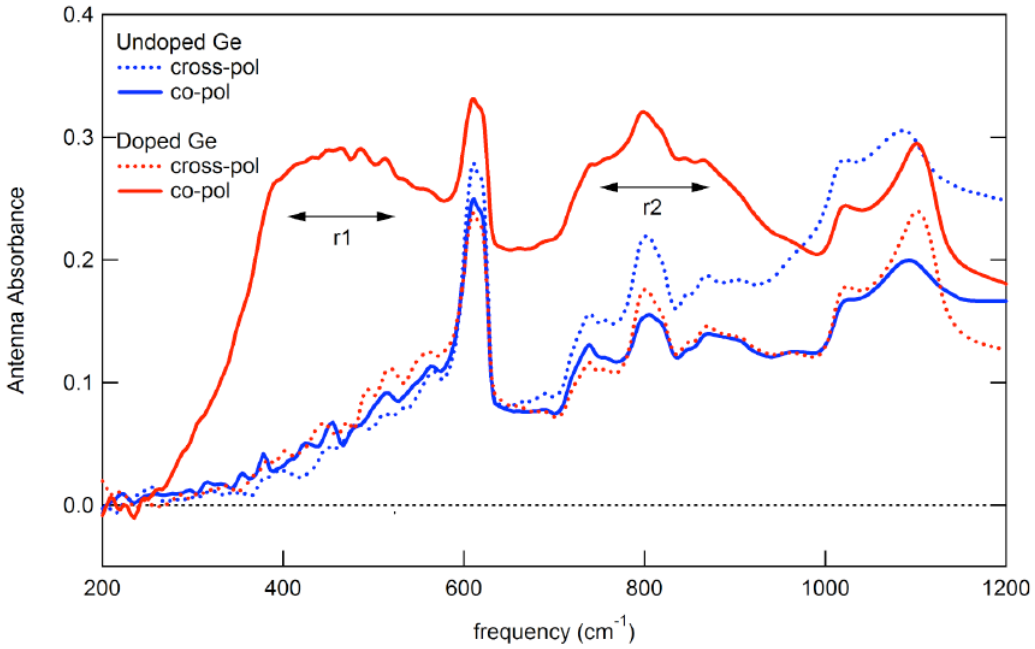

Figure 5. Fourier transform infrared absorbance spectra of fabricated 1 μm thick n-Ge double antenna structures (red). Two broad resonance peaks are clearly labelled R1 and R2 for the co-polarization. The undoped Ge double antenna reference is also displayed (blue).

These results provide an understanding of the plasmonic properties of the n-Ge double antenna. The potential for sensing using a transmission geometry with the double antennas was therefore investigated. The R2 resonance (see **Figure 5**) for the sensing of thin solid-state layers with vibrational fingerprints in the spectral window was demonstrated. This was achieved by using a polydimethylsiloxane (PDMS) layer, which features a vibrational absorption resonance at 800 cm^{-1}. This absorption line matches very well with the spectral position of the R2 near-field resonance. By spin-coating highly diluted PDMS and further curing, we obtained a PDMS thickness below 40 nm [4]. The transmission spectra for the antenna samples are displayed in **Figure 6**. A comparison between the transmission spectra of the clean antennas and of the spin-coated antennas reveals that the PDMS layer induces two changes in the spectra: a slight redshift of the plasmonic resonance, due to the increased refractive index in the antenna surroundings, and the appearance of an asymmetric spectral line around 800 cm^{-1}.

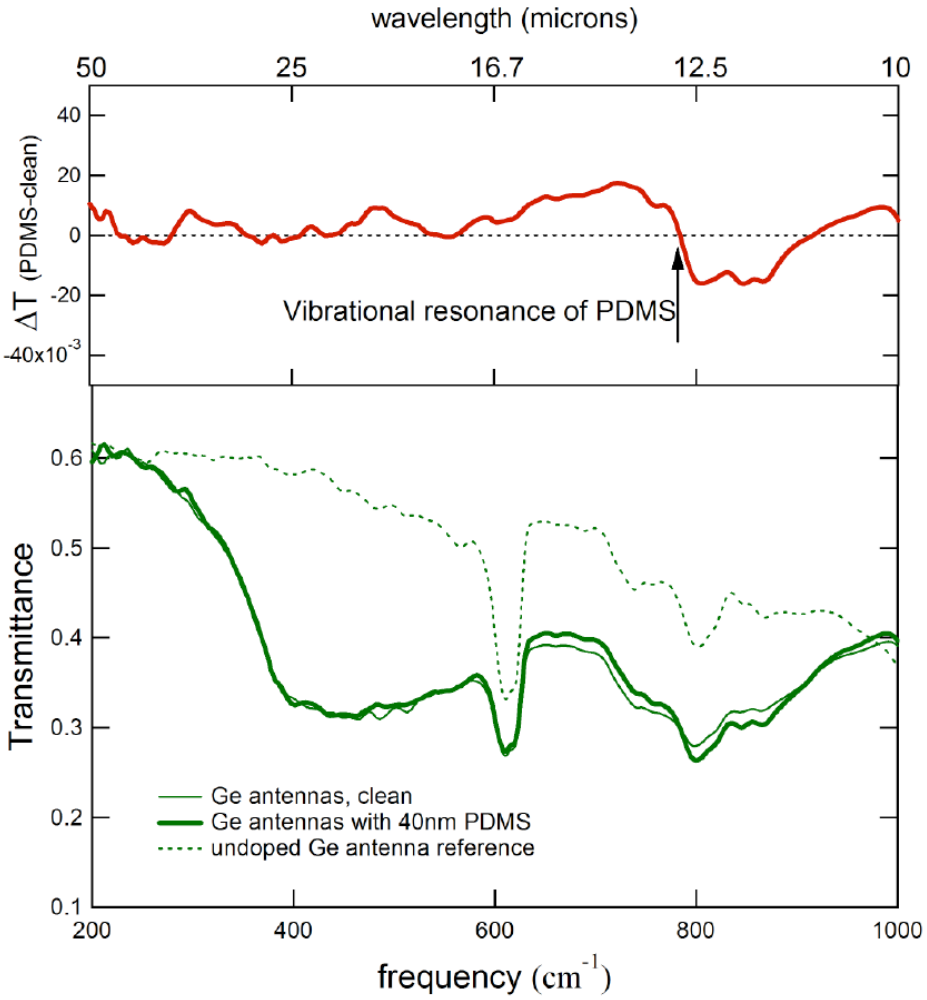

Figure 6. The experimental transmission spectra acquired after PDMS is spin coated onto the double antenna structures (solid lines) and reference spectra from the clean samples. The undoped reference Ge antennas are also displayed (dash line). The upper plot shows the difference transmission spectra obtained after subtraction of the clean n-Ge antennas from antennas coated with PDMS.

Through this experiment, it is demonstrated that the line-shape around 800 cm^{-1} is completely different for parallel and perpendicular polarization and that the line-shape obtained for perpendicular polarization is similar to the one obtained from nominally undoped antenna samples. This observation clearly highlights the electromagnetic coupling between PDMS and the longitudinal plasmon resonances. We also calculated the ratio between the experimental spectra acquired from PDMS-coated antennas with parallel and perpendicular polarization, both for the doped and undoped samples. Noticeably, the 800 cm^{-1} vibrational feature from PDMS completely disappears in the undoped antennas after such normalization, meaning that no PDMS-antenna interaction is taking place irrespective of the field polarization.

CONCLUSIONS

In conclusion, intersubband absorption from 8.1 nm p-Ge QWs designed by an 8-band k.p Poisson-Schrödinger tool has been demonstrated. High quality growth of the Ge QWs has been

confirmed STEM analysis. FTIR transmission spectroscopy displayed absorption peaks corresponding to intersubband transitions between subband states within the QW. This work demonstrates surface-normal intersubband absorption from p-Ge QWs that occurs in the important atmospheric transmission window of 8-13 μm. It is envisaged that such designs could produce surface normal and waveguide coupled photodetectors for spectroscopic sensing in the MIR. In addition, we have demonstrated localized plasmon resonances in n-Ge double antennas and exploited the fabricated devices for sensing experiments based on the resonant detection of molecular vibrational fingerprints of PDMS. This leads to enhancement factors of up to 2 orders of magnitude for the PDMS located in the antenna hotspots. The developed technology holds great promise for the realization of CMOS-compatible mid-IR devices for substance-specific molecular sensing.

ACKNOWLEDGMENTS

The research leading to these results has received funding from the European Union's Seventh Framework Programme under Grant Agreement No. 613055 and U.K. EPSRC (Project No. EP/N003225/1).

REFERENCES

1. A. Rogalski, *J. Appl. Phys.* **93**, 4355 (2003).
2. L. Meriggi, M. J. Steer, Y. Ding, I. G. Thayne, C. MacGregor, C. N. Ironside, and M. Sorel, *J. Appl. Phys.* **117**, 063101 (2015).
3. K. Gallacher, A. Ballabio, R. W. Millar, J. Frigerio, A. Bashir, I. MacLaren, G. Isella, M. Ortolani, and D. J. Paul, *Appl. Phys. Lett.* **108**, 091114 (2016).
4. L. Baldassarre, E. Sakat, J. Frigerio, A. Samarelli, K. Gallacher, E. Calandrini, G. Isella, D. J. Paul, M. Ortolani, and P. Biagioni, *Nano Lett.* **15**, 7225 (2015).
5. R.P.G. Karunasiri, J.S. Park, Y.J. Mii, and K.L. Wang, *Appl. Phys. Lett.* **57**, 2585 (1990).
6. J. S. Park, R. P. G. Karunasiri, and K. L. Wang, *Appl. Phys. Lett*. **61**, 681 (1992).
7. M. De Seta, G. Capellini, Y. Busby, F. Evangelisti, M. Ortolani, M. Virgilio, G. Grosso, G. Pizzi, A. Nucara, and S. Lupi, *Appl. Phys. Lett.* **95**, 051918 (2009).
8. D.J. Paul, *Laser & Photon. Rev.* **4**, 610 (2010).
9. G. Isella, D. Chrastina, B. Rössner, T. Hackbarth, H.-J. Herzog, U. König, and H. von Känel, *Solid-State Electron.* **48**, 1317 (2004).
10. S. Cecchi, E. Gatti, D. Chrastina, J. Frigerio, E. Müller Gubler, D.J. Paul, M. Guzzi, and G. Isella, *J. Appl. Phys.* **115**, 093502 (2014).
11. P. Boucaud, L. Wu, F. Julien, J.-M. Lourtioz, I. Sagnes, Y. Campidelli, and P.-A. Badox, *Appl. Surface Sci.* **102**, 342 (1996).
12. P. Kruck, M. Helm, T. Fromherz, G. Bauer, J. F. Nützel, and G. Abstreiter, *Appl. Phys. Lett.* 69, 3372 (1996).
13. D.J. Paul, *Phys. Rev. B* **77**, 155323 (2008).
14. R. C. Newman, *J. Phys.: Conden. Matter* **12**, R335 (2000).
15. T. Kotani, M. Arita, K. Hoshino, and Y. Arakawa, *Appl. Phys. Lett.* **108**, 052102 (2016).
17. P. Biagioni, J.-S. Huang, and B. Hecht, *Reports Prog. Phys.* **75**, 024402 (2012).
18. V. Giannini, A. I. Fernandez-Domınguez, S. C. Heck, and S. A. Maier, *Chem. Revs.* **111**, 3888 (2011).

19. S. Lal, S. Link, and N. J. Halas, *Nature Photon.* **1**, 641 (2007).
20. L. Novotny and N. van Hulst, *Nature Photon.* **5**, 83 (2011).
21. R. Zia, J. A. Schuller, A. Chandran, and M. L. Brongersma, *Mat. Today* **9**, 20 (2006).
22. F. Neubrech, A. Pucci, T. W. Cornelius, S. Karim, A. Garcıa-Etxarri, and J. Aizpurua, *Phys. Rev. Lett.* **101**, 157403 (2008).
23. R. Adato, A. Artar, S. Erramilli, and H. Altug, *Nano Letters* **13**, 2584 (2013).
24. R. Adato, A. A. Yanik, J. J. Amsden, D. L. Kaplan, F. G. Omenetto, M. K. Hong, S. Erramilli, and H. Altug, *Proc. National Acad. Sci.* **106**, 19227 (2009).
25. O. Limaj, S. Lupi, F. Mattioli, R. Leoni, and M. Ortolani, *Appl. Phys. Lett.* **98**, 091902 (2011).
26. A. Samarelli, D. S. Macintyre, M. J. Strain, R. M. De La Rue, M. Sorel, and S. Thoms, *J. Vac. Sci. Technol. B* **26**, 2290 (2008).
27. M. M. Mirza, H. Zhou, P. Velha, X. Li, K. E. Docherty, A. Samarelli, G. Ternent, and D. J. Paul, *J. Vac. Sci. Technol. B* **30**, 06FF02 (2012).
28. M. M. Mirza, D. A. MacLaren, A. Samarelli, B. M. Holmes, H. Zhou, S. Thoms, D. MacIntyre, and D. J. Paul, *Nano Letters* **14**, 6056 (2014).